Noda *Earth, Planets and Space* (2022) 74:89
https://doi.org/10.1186/s40623-022-01649-8

Earth, Planets and Space

FULL PAPER Open Access

Dynamic earthquake sequence simulation with an SBIEM accounting for interseismic poroelastic rebound

Hiroyuki Noda*

Abstract

Afterslip inside a coseismic slip patch is rarely observed, though some previous studies suggest that it is driven by poroelastic rebound (PER). These studies assume constant frictional strength, whereas time-dependent strengthening (healing) of a fault is expected from laboratory experiments, which provide a basis for a rate- and state-dependent friction law (RSF). In this study, quasistatic poroelasticity (PE) was implemented in a dynamic earthquake sequence simulation using a spectral boundary integral equation method, and the effect of PER on the behavior of a fault governed by RSF was examined. Spatio-temporal convolution for PE would significantly affect the resolution of the numerical simulation affordable. This problem has been resolved by numerical approximation of the time dependency of Green's function of PE in the wavenumber domain, definition of memory variables, and reformulation of the temporal convolution into ordinary differential equations of them. In the novel method, the additional numerical costs due to PE are negligible. A planar fault with a rate-weakening patch embedded in the rate-strengthening region was simulated. Because it is the healing of the fault that competes against PER, both the aging law and slip law were examined, which have different characteristics in the evolution of the fault strength. The simulation results indicate that PER causes postseismic loading to the patch, but the healing efficiently suppresses afterslip not only for the aging law, but also for the slip law. When cases with different friction laws are compared, the healing is more significant for the aging law, which has log-t strengthening at a limit of $V \to 0$. However, the effect of PER on the slip rate is minor for the slip law. The slip law yields additional healing if the fault is accelerated by loading owing to PER. The simulation results are consistent with the absence of afterslip within the coseismic slip patches in the observations.

Keywords: Poroelasticity, Numerical simulation, Earthquake sequence, SBIEM, Fault healing, Afterslip

*Correspondence: noda.hiroyuki.7z@kyoto-u.ac.jp

Disaster Prevention Research Institute, Kyoto University, Gokasho, Uji 6110011, Japan

Graphical Abstract

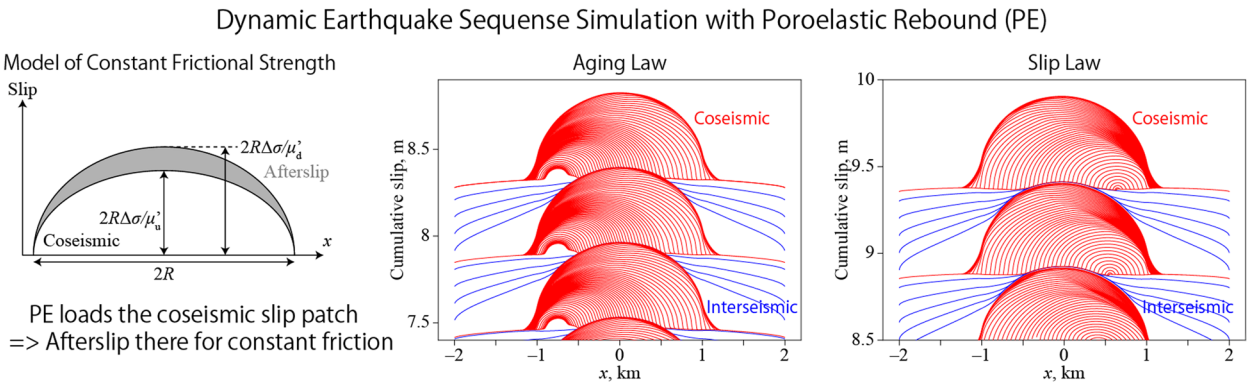

Healing of a fault dominates over PE, suppressing afterslip inside the patch for both the aging law and slip law.

Introduction

Afterslip, which follows a dynamic earthquake rupture and can cause aftershocks (Hsu et al. 2006), takes place in the vicinity of a coseismic slip patch (e.g., Miyazaki et al. 2004). The afterslip inside the patch has rarely been confirmed. Geodetic inversion sometimes yields an afterslip distribution that apparently overlaps with a coseismic slip distribution, but the resolution check (e.g., the checkerboard test) indicates that it may be an artifact (e.g., Meneses-Gutierrez et al. 2019). The distribution of small repeating earthquakes (e.g., Kato and Igarashi 2012) more clearly shows that regions of afterslip and coseismic slip are separated. Earthquake sequence simulation for a fault governed by the rate- and state-dependent friction law (RSF) (Dieterich 1979; Ruina 1983) in an elastic medium typically yields the invasion of afterslip into the patch, but the core of the patch remains locked until the next earthquake (e.g., Tse and Rice 1986; Scholz 1998; Lapusta et al. 2000).

On the other hand, some previous theoretical and numerical studies have suggested the possibility of afterslip even inside the coseismic slip patch driven by the poroelastic effect. Rapid, undrained deformation due to earthquake rupture causes heterogeneity in the volumetric strain and pore pressure p in the surrounding poroelastic medium. This causes fluid flow, diffusion of p, and associated poroelastic deformation, referred to as poroelastic rebound (PER) (e.g., Peltzer et al. 1996). For an isotropic medium, the undrained and drained responses have the same shear modulus μ and different Poisson's ratios $\nu_u > \nu_d$, where the subscripts $_u$ and $_d$ indicate the undrained and drained conditions, respectively.

Detournay and Cheng (1991) demonstrated that instantaneous opening of a drained crack of a fixed length ("mode 1" in their paper) is followed by additional time-dependent opening due to PER. The similarity between an in-plane shear crack and an open crack in the static limit suggests an afterslip due to the PER (Fig. 1). Coseismic, rapid stress drop $\Delta\sigma$ causes slip distribution scaled by the inverse of the stiffness in the undrained limit μ_u'. For example, a two-dimensional (2-D) linear shear crack of length $2R$ in an in-plane problem hosts a maximum slip of $2R\Delta\sigma/\mu_u' = 2(1-\nu_u)R\Delta\sigma/\mu$. In the limit of a sufficiently large time, the stiffness in the drained limit μ_d' is important. In the example of the 2-D crack (Knopoff 1958), the maximum slip is given by $2R\Delta\sigma/\mu_d' = 2(1-\nu_d)R\Delta\sigma/\mu$. The difference between them $2(\nu_u-\nu_d)R\Delta\sigma/\mu$ is generated as an afterslip. Yamashita (2007) and Yamashita and Suzuki (2009) studied the case with differences in poroelastic properties across the fault, and suggested afterslip even within the coseismic slip patch and postseismic crack extension due to PER (Table 1).

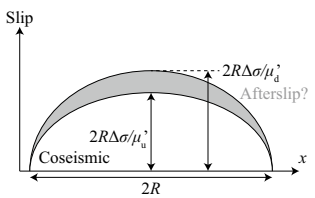

Fig. 1 Difference in the undrained and the drained responses for uniform stress drop $\Delta\sigma$. Afterslip due to PE expected for an inplane shear crack with constant frictional strength is indicated in grey

Table 1 Physical properties used in the simulations

Poroelastic properties		
Shear wave speed	c_s	3 km/s
Shear modulus	μ	30 GPa
Biot's stress coefficient	α	0.47*
Undrained Poisson's ratio	ν_u	0.34*
Drained Poisson's ratio	ν_d	0.25*
Diffusion coefficient	c	Variable
Frictional properties		
Direct effect parameter	A	1MPa
Evolution effect parameter	B	$1.5\text{MPa}(\lvert x\rvert \le R)$
		$0(\lvert x\rvert \ge 1.1R)$
Aging law		
State-evolution slip distance	L^{ag}	$[0.15\pi(1-\nu_u)(B-A)^2/b\mu]R$
Modified slip law		
State-evolution slip distance	L^{sl}	$2\times10^{-6}R$
Characteristic time	t_c	$L^{sl}/(1\text{ m/s})$

* Properties for granite in Wang (2001)

The other poroelastic properties appearing in the main text (M and κ) can be expressed in terms of the properties listed here. Parameter studies in terms of c were conducted

These models assume a constant interface strength, whereas laboratory friction experiments show an increase in the fault strength (healing) with the time of stationary contact after slip ceases (Dokos 1946; Dieterich 1972), as is realized by the RSF (e.g., Marone 1998). In this study, quasistatic poroelasticity (PE) was implemented in a dynamic earthquake sequence simulation (e.g., Lapusta et al. 2000) accounting for elastic wave propagation using a spectral boundary integral equation method (SBIEM), and its consequences on the fault behavior were investigated. Note that there are a number of recent studies on poroelastic effect on a fault governed by the RSF. Jha and Juanes (2014) developed a quasistatic model for RSF faults embedded in poroelastic medium with multiphase flow. Torberntsson et al. (2018) carried out quasidynamic earthquake sequence simulations for an RSF fault in poroelastic medium with a permeable shear zone, and demonstrated an earthquake rupture induced by fluid injection. A similar finite difference approach was taken by Heimisson et al. (2019) to study aseismic transients in a shape of slow slip pulses under the quasidynamic assumption. A linearized stability analysis of a RSF fault in a poroelastic medium allowing dilatancy and compaction in the fault zone was presented in Heimisson et al. (2021). Although PER should operate actively in just after earthquakes, postseismic behavior has not been reported in detail.

Linear PE is assumed here for simplicity. Linearity allows us to calculate the quasistatic deformation due to PE by spatio-temporal convolution of the slip history and Green's function. On the other hand, in the dynamic earthquake sequence simulation developed by Rice and Ben-Zion (1996) for an elastic medium, dynamic, wave-mediated stress transfer is calculated by spatio-temporal convolution of the slip history and Green's function of elastodynamics. The computational costs and storage of history for this calculation are limiting factors for the problem size given the restricted computational resources. The additional spatiotemporal convolution for PE significantly affects the resolution of the fault affordable. Miyake and Noda (2019) addressed this problem for a Maxwell-viscoelastic medium by defining a memory variable and reformulating the temporal convolution into an ordinary differential equation (ODE) of the memory variable. Note that Ruina (1983) took a similar approach in formulating the rate- and state-dependent friction law. This method enabled the implementation of quasistatic viscoelastic relaxation in a dynamic earthquake sequence simulation without significant additional cost. In this study, PE was implemented using a similar method by introducing 18 memory variables for each discrete wavenumber without conducting a temporal convolution.

A simple fault model with one rate-weakening patch embedded in the rate-strengthening region was simulated. The postseismic strengthening of the patch is a key process that competes against PER. Therefore, both the aging law and slip law were tested, which have different characteristics in the state evolution (Marone 1998). A fault within a uniform poroelastic medium was considered in this paper. The short-time response within a coseismic time scale was assumed to be given by the undrained response. Such assumption cannot be realistic for a fault between dissimilar materials (e.g., Rudnicki and Rice 2006; Dunham and Rice 2008). Note that attenuation and dispersion of elastic waves due to wave-induced fluid flow are neglected. Undrained cases were first simulated, and then simulations with PE with different characteristic diffusion times were conducted. Based on the simulation results, the possibility of enhancement of afterslip due to PER is discussed.

Methodology

Poroelastic Green's function in the SBIEM

A planar fault embedded in a linearly poroelastic infinite medium is considered. To concentrate our focus on the effect of PER, dilatancy and compaction due to deformation of fault gouge (e.g.,, Heimisson et al. 2021) are neglected. Because it is the volumetric strain ϵ_{kk} that causes the pore pressure change p and the subsequent fluid

flow, PE is not important in anti-plane problems. Therefore, the focus of this study was on in-plane problems. The new method proposed here can be readily applied to the 3-D problem of a planar fault, because it the convolution kernel for such a problem can be constructed by the combination of those for 2-D in-plane and anti-plane problems (Geubelle and Rice 1995; Lapusta and Liu 2009).

In an elastodynamic problem with a fault, shear traction on a fault τ at location x and time t can be expressed as follows (Cochard and Madariaga 1994; Geubelle and Rice 1995):

$$\tau(x,t) = \tau_0(x,t) + \phi - \frac{\mu}{2c_s}V(x,t), \tag{1}$$

where τ_0 is the traction realized at a reference state without any slip on the fault, ϕ is the wave-mediated stress transfer due to previous fault motion, V is the slip rate, μ is the shear modulus, and c_s is the shear wave speed. The final term in Eq. (1) represents the impedance effect, which is sometimes referred to as the radiation damping effect (Rice 1993). Rice and Ben-Zion (1996) split ϕ into the following two terms:

$$\phi = \phi_{st} + \phi_{dy}, \tag{2}$$

where ϕ_{st} is the static traction change, which would be achieved if the fault were instantaneously welded up and elastic waves radiated out of the system. ϕ_{dy} is simply defined as $\phi_{dy} = \phi - \phi_{st}$. In the elastic case, ϕ_{st} depends only on the current slip distribution, and ϕ_{dy} is calculated by the spatiotemporal convolution of V and Green's function with truncation in terms of the delay time. The time window for the convolution t_w is taken as the time for which the shear wave travels several times the system size (coseismic timescale). In an in-plane problem, the Fourier transform of ϕ_{st} is expressed as follows:

$$\Phi_{st}(k,t) = \int_{-\infty}^{\infty} \phi_{st}(x,t)e^{-ikx}dx = -\frac{|k|\mu'}{2}D(k,t), \tag{3}$$

where μ' is expressed by μ and the Poisson ratio ν as

$$\mu' = \frac{\mu}{1-\nu}, \tag{4}$$

and D is the Fourier transform of slip the δ

$$D(k,t) = \int_{-\infty}^{\infty} \delta(x,t)e^{-ikx}dx. \tag{5}$$

In this study, it was assumed that the fluid flow was negligible in the coseismic timescale; ϕ_{dy} was calculated in the same manner as in previous studies for an elastic medium (e.g., Lapusta et al. 2000) with the undrained properties. ϕ_{st} is modified to ϕ_{st}^{PE} to account for the PE. The constitutive law of linear poroelasticity is as follows:

$$\sigma_{ij} = C_{ijkl}\epsilon_{ij} - \alpha_{ij}p, \tag{6}$$

$$p = M\left(\zeta - \alpha_{ij}\epsilon_{ij}\right), \tag{7}$$

$$q_i = -\kappa_{ij}p_{,j}, \tag{8}$$

$$\frac{\partial\zeta}{\partial t} + q_{i,i} = 0. \tag{9}$$

Equations (6) and (7) are the stress–strain relations accounting for the changes in p and in the fluid content ζ, where σ_{ij} is the stress, ϵ_{ij} is the strain, C_{ijkl} is the drained elastic modulus, α_{ij} is the Biot stress coefficient, and M is the Biot modulus. Equation (8) is Darcy's law, where q_i is volumetric flux of the fluid, κ_{ij} is the mobility of the fluid given by the permeability of the medium divided by the viscosity of the fluid k_{ij}/η. Equation (9) is the mass conservation law for the pore fluid. For simplicity, the medium is assumed to be isotropic. In this case, the degrees of freedom of the tensorial rock properties are significantly reduced, such that C_{ijkl} is expressed in terms of the shear modulus μ and the drained Poisson ratio ν_d, $\alpha_{ij} = \alpha$, and $\kappa_{ij} = \kappa = k/\eta$.

Cheng and Detournay (1998) presented a spatiotemporal stress change due to a sudden, spatially concentrated slip $\delta(x,t) = \delta_D(x)H(t)$ (Appendix D.11 in their paper). δ_D is the Dirac's delta function, and H is the Heaviside function. Evaluating the corresponding shear traction on the fault, we obtain Green's traction function for a concentrated slip τ^G as follows:

$$\tau^G(x,t) = \frac{H(t)}{2\pi x^2}\left\{\mu_u' + \Delta\mu'\left[3\frac{1-e^{-x^2/4ct}}{x^2/4ct} - 2e^{-x^2/4ct}\right]\right\}. \tag{10}$$

where μ_u' and $\Delta\mu'$ are the effective on-fault rigidity under undrained conditions and the difference between the drained and undrained conditions, respectively, and are given by

$$\mu_d' = \frac{\mu}{1-\nu_d}, \mu_u' = \frac{\mu}{1-\nu_u}, \Delta\mu' = \mu_d' - \mu_s', \tag{11}$$

where ν_u is the undrained Poisson ratio

$$\nu_u = \frac{1}{2}\left(1 - \frac{\mu(1-2\nu_d)}{M\alpha^2(1-2\nu_d)+\mu}\right), \tag{12}$$

where c is the diffusion coefficient of p given by

$$c = \frac{2\kappa\mu(\nu_u-\nu_d)(1-\nu_d)}{\alpha^2(1-\nu_u)(1-2\nu_d)^2}. \tag{13}$$

Using Green's function τ^{G}, the static part of the traction change accounting for PE $\phi_{\mathrm{st}}^{\mathrm{PE}}$ can be expressed as follows:

$$\phi_{\mathrm{st}}^{\mathrm{PE}}(x,t) = \left[\int_{-\infty}^{\infty} \mathrm{d}x' \int_{-\infty}^{t} \mathrm{d}t'\right] V\left(x',t'\right)\tau^{\mathrm{G}}\left(x-x',t-t'\right). \tag{14}$$

Fourier transformation leads to

$$\begin{aligned}\Phi_{\mathrm{st}}^{\mathrm{PE}}(k,t) &= \int_{-\infty}^{\infty} \phi_{\mathrm{st}}^{\mathrm{PE}}(x,t)\mathrm{e}^{-\mathrm{i}kx}\mathrm{d}x \\ &= \left[\int_{-\infty}^{t} \mathrm{d}t'\right] \dot{D}\left(k,t'\right) T^{\mathrm{G}}\left(k,t-t'\right),\end{aligned} \tag{15}$$

where a dot represents time derivative, and T^{G} is the Fourier transform of τ^{G}

$$\begin{aligned}T^{\mathrm{G}}(k,t) &= \int_{-\infty}^{\infty} \tau^{\mathrm{G}}(x,t)\mathrm{e}^{-\mathrm{i}kx}\mathrm{d}x \\ &= -\frac{|k|\mu_{\mathrm{u}}'}{2}\left[1+\frac{\Delta\mu'}{\mu_u'}\left(1-F\left(ctk^2\right)\right)\right].\end{aligned} \tag{16}$$

Note that $H(t)$ was eliminated, because $T^G(k,t)$ only in $t>0$ is important. F is a universal function that is independent of the material properties:

$$F(s) = (1+2s)\mathrm{erfc}\left(\sqrt{s}\right) - \frac{2}{\sqrt{\pi}}\sqrt{s}\mathrm{e}^{-s}. \tag{17}$$

Song and Rudnicki (2017) derived a Green's function for a dislocation in a poroelastic medium with "leaky" fault plane, which has a resistance (fluid flux per pore pressure gap across the fault plane). It is a generalization of the solution by Cheng and Detournay (1998), and may substitute the Green's function used here to study the effect of impermeable, caly-rich fault.

Implementation using memory variables

A direct evaluation of Eq. (15) requires storage of the slip rate history in the past, which requires significant additional computational resources. Miyake and Noda (2019) resolved this problem by reformulating the temporal convolution into an ODE of a memory variable, the Fourier-transformed effective slip D_{eff}. In this study, the effective slip was defined based on the undrained mechanical response as follows:

$$\Phi_{\mathrm{st}}^{\mathrm{PE}}(k,t) = -\frac{|k|\mu_{\mathrm{u}}'}{2} D_{\mathrm{eff}}(k,t). \tag{18}$$

From Eqs. (15), (16), and (18), D_{eff} is expressed as follows:

$$D_{\mathrm{eff}} = \int_{-\infty}^{t} \dot{D}\left(k,t'\right)\left[1+\frac{\Delta\mu'}{\mu_{\mathrm{u}}'}\left(1-F\left(c\left(t-t'\right)k^2\right)\right)\right]dt'. \tag{19}$$

For Maxwell viscoelasticity in antiplane problems, Miyake and Noda (2019) found a simple ODE of D_{eff}. A similar formulation is possible for Maxwell viscoelasticity in in-plane problems (under preparation) and most likely for many other linear rheologies. For poroelasticity, an ODE equivalent to Eq. (19) could not be found so that a numerical approximation was developed.

Figure 2a, b shows $F(s)$ in linear and logarithmic vertical scales, respectively. Note that $F(s)$ represents the transition between the undrained ($F(0)=1$) and drained ($F(\infty)=0$) responses. $F(s)$ is a monotonically decaying function and becomes smaller than 10^{-6} by the non-dimensional time $s=10$. If it can be approximated as follows:

$$F(s) \approx \sum_{i=1}^{n} a_i \exp\left(-\frac{s}{s_i}\right), \tag{20}$$

Equation (19) then becomes

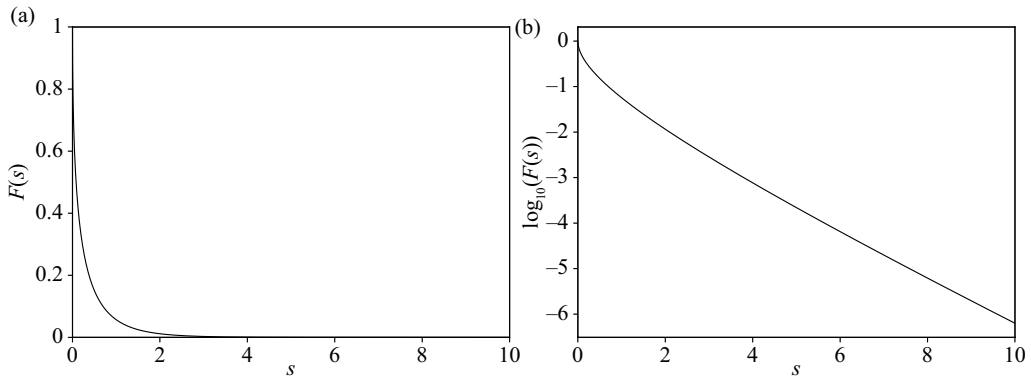

Fig. 2 Plots of **a** $F(s)$ and **b** $\log_{10}(F(s))$, which represent transition between undrained to drained responses

$$D_{\text{eff}} \approx \int_{-\infty}^{t} \dot{D}\left(k,t'\right)\left[1+\frac{\Delta\mu'}{\mu'_{\text{u}}}\left(1-\sum_{i=1}^{n} a_i \exp\left(-\frac{c\left(t-t'\right)k^2}{s_i}\right)\right)\right]dt' = \left(1+\frac{\Delta\mu'}{\mu'_{\text{u}}}\right)D\left(k,t'\right)-\frac{\Delta\mu'}{\mu'_{\text{u}}}\sum_{i=1}^{n} a_i D_i(k,t), \tag{21}$$

where D_i represents additional memory variables defined as follows:

$$D_i(k,t) = \int_{-\infty}^{t} \dot{D}\left(k,t'\right)\exp\left(-\frac{c\left(t-t'\right)k^2}{s_i}\right)dt'. \tag{22}$$

Equation (22) can be reformulated into an ODE for each i as follows:

$$\dot{D}_i(k,t) = \dot{D}(k,t) - \frac{ck^2}{s_i}D_i(k,t). \tag{23}$$

This can be easily integrated every time step.

Each memory variable D_i has its weight of contribution $-a_i\Delta\mu'/\mu'_{\text{u}}$ to the Fourier-transformed effective slip D_{eff} and its non-dimensional characteristic decay time s_i. a_i and s_i for $i = 1, 2, \ldots, n$ are determined by least-squares fitting of Eq. (20) to discretely sampled data $\{F(0.01), F(0.02), \ldots, F(10)\}$ under the constraint $\sum_{i=1}^{n} a_i = 1$. The residual decreases as n increases (Fig. 3), and the absolute approximation error becomes less than 10^{-6} with $n = 18$, which is adopted in the applications described later in this paper.

There were 18 memory variables for each wavenumber, and the number of collocation points in the wavenumber domain was approximately the same as the number of spatial grid points. The uniform mode does not contribute to the shear stress and need not be considered. Noda and Lapusta (2010) used approximately 120 memory or state variables for each point on the fault to express the frictional heating and thermal pressurization of the pore fluid. The time integration of these variables does not result in a significant additional computational cost. Indeed, in the examples shown later, the computational time for a sequence of 20 earthquakes may be shorter in cases with PE relative to the undrained case. This is because PER decreases the recurrence interval. The proposed method was found to be quite efficient.

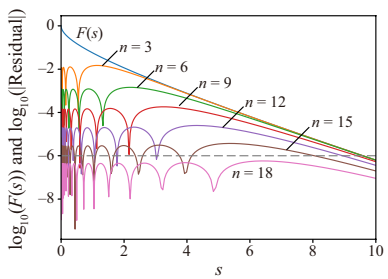

Fig. 3 $F(s)$ and the residual of the numerical approximation of $F(s)$ (Eq. (20)). The absolute error was less than 10^{-6} with $n = 18$

The time integrations of slip δ, its Fourier transform D and a state variable in a rate- and state-dependent friction law in the dynamic earthquake sequence simulation by Noda and Lapusta (2010) are based on the assumption of piecewise constant V over time. Here, the time integration of memory variables D_i is performed exactly in the same manner, with an unconditionally stable second-order accurate predictor–corrector method based on an exponential time differencing method. Note that the characteristic decay time s_i/k^2c is so small for high-wavenumber components that explicit time integration based on a constant time derivative is unrealistic in the simulation of interseismic periods. For details, please refer to Noda and Lapusta (2010), in which a similar technique was adopted to simulate the diffusion of temperature and pore pressure normal to the fault.

Problem setting of example problems

System geometry

Let us select length, speed, and stress as the three independent dimensions and consider appropriate scales relevant to natural earthquakes. Earthquakes occur in a vastly wide range of length scales, as recognized by the Gutenberg–Richter law. In addition, the permeability κ has the dimension of squared length and is known to vary for orders of magnitude depending on the rock type. Therefore, the length scale of the problem shall not be specified at this point. The variation in the elastic property of rock is minor compared to them. Therefore, the scales of speed and stress are specified in the example problems described below by setting $c_{\text{s}} = 3\,\text{km/s}$ and $\mu = 30$ GPa. Biot's stress coefficient α, undrained and drained Poisson's ratios ν_{u} and ν_{d} were set $\alpha = 0.47$, $\nu_{\text{u}} = 0.34$, $\nu_{\text{d}} = 0.25$, respectively, based on the values for granite in Wang (2001). The parameters used in the example simulations are listed in Table 1.

The effect of PER was investigated for a simple problem setting: a planar fault governed by RSF (Dieterich 1979; Ruina 1983) with a rate-weakening patch. The frictional resistance at steady state is as follows:

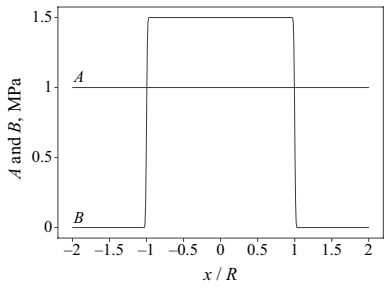

Fig. 4 Distributions of frictional parameters A and B

$$\tau_{\rm ss} = \tau_* + (A-B)\ln\left(\frac{V}{V_*}\right), \tag{24}$$

where τ_* is the steady-state frictional resistance at the reference $V = V_*$, and $A - B$ represents the steady-state rate dependency. Note that the value of τ_* is insignificant, as a linear poroelastic material is considered; spatial variation in τ_* is absorbed by definition of the initial or reference state from which the slip δ is measured. A and B are the amounts of direct and evolution effects, respectively. The rate-weakening patch is expressed using a smoothed boxcar function (The SCEC/USGS Spontaneous Rupture Code Verification Project, TPV105; Noda and Lapusta 2010):

$$\mathrm{sbox}(x;W,w) = \begin{cases} 1 & (|x| \le W) \\ \frac{1}{2}\left[1+\tanh\left(\frac{w}{|x|-W-w}+\frac{w}{|x|-W}\right)\right] & (W \le |x| \le W+w) \\ 0 & (|x| \ge W+w) \end{cases}, \tag{25}$$

as (Fig. 4)

$$A = 1\mathrm{MPa}, B = 1.5\mathrm{sbox}(x;R,0.1R)\mathrm{MPa}. \tag{26}$$

These values are consistent with effective normal stress about 100 MPa.

The fault is driven by prescribing a long-term constant slip rate $V_{\rm pl} = 10^{-9}$m/s in $|x| > 2R$. $V_{\rm pl}$ constrains the long-term slip rate of the fault and was adopted as the reference, $V_* = V_{\rm pl}$. Noda (2021) developed a dynamic earthquake sequence simulation using an SBIEM without a periodic boundary condition based on the method of Cochard and Rice (1997). This method is only applicable if the source of the traction change is supported within a certain region. Here, the effective elastostatic source is the inverse Fourier transform of $D_{\rm eff}$, which may not be constrained within $|x| < 2R$. Therefore, removal of the periodic boundary condition may be difficult. In the example problems, periodic boundaries are assumed every $16R$, four times the length of the segment governed by the RSF law. This is sufficiently long such that the effect of the periodic boundary is modest (Lapusta et al. 2000; Noda 2021). The time window $t_{\rm w}$ for the calculation $\phi_{\rm dy}$ was set to $12R/c_{\rm s}$.

Friction law

Both the aging law and the slip law are examined as follows:

$$\begin{aligned} \tau &= \tau_* + A\ln\left(\frac{V}{V_*}\right) + B\ln(\theta) \\ \dot\theta &= \frac{V}{L}\left(\frac{V_*}{V} - \theta\right) \end{aligned} \quad \text{(aging law)}, \tag{27}$$

and

$$\begin{aligned} \tau &= \tau_* + A\ln\left(\frac{V}{V_*}\right) + \Theta \\ \dot\Theta &= \frac{V}{L}(\tau_{\rm ss} - \tau) \end{aligned} \quad \text{(slip law)}. \tag{28}$$

where L is the characteristic slip of the state evolution, θ is the state variable in the aging law representing recent nondimensional slowness, and Θ is the state variable in the slip law representing the frictional strength relative to the reference ($\tau - \tau_*$ at $V = V_*$). The aging law provides more efficient healing of the fault than the slip law as follows (Marone 1998):

$$\lim_{V\to 0}\dot\theta = \frac{V_*}{L}, \lim_{V\to 0}\dot\Theta = 0. \tag{29}$$

At the rupture front, the aging law results in an almost linear slip weakening of the slope $-\mathrm{d}\tau/\mathrm{d}\delta \approx B/L$, while the slip law causes exponential slip weakening towards the residual frictional strength (Ampuero and Rubin 2008), which causes a much larger $-\mathrm{d}\tau/\mathrm{d}\delta$. In preliminary simulations with constant L (not shown in this paper), the dynamic earthquake sequence simulation with the slip law requires large computational resources and produces a series of supershear ruptures, which may not be realistic. To produce comparable earthquake sequences of sub-Rayleigh ruptures between the aging law and slip law, and to enable parameter study in terms of the fluid mobility κ for affordable computational costs, L is increased at the coseismic slip rate for the slip law, while it is kept constant for the aging law as follows:

$$L = \begin{cases} L^{\rm ag} & (\text{Aging law}) \\ L^{\rm sl} + Vt_{\rm c} & (\text{Slip law}) \end{cases}. \tag{30}$$

This modification leads to a time-weakening model at high enough slip rate $V \gg L^{\rm sl}/t_{\rm c}$ for the slip law with the

characteristic time t_c.The fracture energy increases as the peak slip rate increases, and the length of the process zone is kept finite even after a rupture grows extensively. Andrews (2004) used a time-weakening friction in simulation of dynamic rupture to account for increasing fracture energy with rupture size. Note that this modification is not meant to make the simulation "realistic" regarding complex physical and chemical effects activated at coseismic slip rates (e.g., Di Toro et al. 2011). The healing of the fault after an earthquake rupture may rule out afterslip driven by the PER. Thus, a comparison of the effect of PER is important between a fault governed by the aging law and that governed by the slip law at a low quasistatic slip rate.

L^{ag} is selected such that the nucleation radius R_c (Rubin and Ampuero 2005) at the undrained condition becomes as follows:

$$R_c = \frac{1}{\pi}\frac{B}{(B-A)^2}\frac{\mu}{1-\nu_u}L^{ag} = 0.15R. \tag{31}$$

This yields $L^{ag} = 1.73 \times 10^{-6}R$. This is small enough for the rate-weakening patch to accommodate nucleation, so that a compact region of acceleration appears prior to an earthquake rupture (e.g., Chen and Lapusta 2009; Noda and Hori 2014). The length scale of the process zone (Lapusta and Liu 2009) is as follows:

$$\Lambda_0^{ag} = \frac{9\pi}{32}\frac{\mu}{1-\nu_u}\frac{L^{ag}}{B} = 4.63 \times 10^{-2}R. \tag{32}$$

To resolve the process zone of the rupture front, the interval of the grid points Δx^{ag} is selected as $\Delta x^{ag} = 4R/512 = 7.81 \times 10^{-3}R$ such that $\Lambda_0^{ag}/\Delta x^{ag} = 5.93$. The interval between the periodic boundaries, $16R$ is discretized by 2,048 grid points.

In example problems with the slip law, L^{sl} is selected as $L^{sl} = 2 \times 10^{-6}R$. The characteristic time t_c is selected as follows:

$$t_c = \frac{L_{sl}}{1\,\mathrm{m/s}}. \tag{33}$$

The Rayleigh wave speed for the undrained Poisson's ratio $\nu_u = 0.34$ is approximately as follows:

$$c_R = 9.34 \times 10^{-1}c_s. \tag{34}$$

For a rupture of this terminal speed, the corresponding length scale of the process zone is as follows:

$$\Lambda_R = c_R t_c = 5.60 \times 10^{-3}R. \tag{35}$$

Ampuero and Rubin (2008) showed that a length scale inversely proportional to B plays an important role in nucleation with the slip law. With the present parameter selection, it becomes as follows:

$$L_b = \frac{\mu}{1-\nu_u}\frac{L^{sl}}{B} = 6.06 \times 10^{-2}R. \tag{36}$$

If a point on the fault is in a steady state at V_{pl} and accelerates owing to stress concentration up to V_{dy}, then Eqs. (28) and (30) yield the maximum slope of the slip weakening as follows:

$$-\frac{d\tau}{d\delta} = \ln\left(\frac{V_{dy}}{V_{pl}}\right)\frac{B}{L^{sl}+V_{dy}t_c} = \ln\left(\frac{V_{dy}}{V_{pl}}\right)\left(1+\frac{V_{dy}}{1\,\mathrm{m/s}}\right)^{-1}\frac{B}{L^{sl}}. \tag{37}$$

The corresponding on-fault length scale of the process zone is as follows:

$$\Lambda_0^{sl} = \frac{9\pi}{32}L_b\left(\ln\left(\frac{V_{dy}}{V_{pl}}\right)\right)^{-1}\left(1+\frac{V_{dy}}{1\,\mathrm{m/s}}\right). \tag{38}$$

This has the minimum value achieved at $V_{dy} = 5.92 \times 10^{-2}$ m/s, generating:

$$\Lambda_0^{sl} \geq 5.23 \times 10^{-2}L_b = 3.17 \times 10^{-3}R. \tag{39}$$

Compared to Eq. (35), modification of L (Eq. (30)), and the selection of the present frictional parameters makes the resolution of the propagating rupture front easier than the nucleation of the earthquake ruptures. The interval of the grid points Δx^{sl} is selected as $\Delta x^{sl} = 4R/4{,}096 = 9.77 \times 10^{-4}R$ so that $\Lambda_0^{sl}/\Delta x = 3.25$. The interval between the periodic boundaries, $16R$ is discretized by 16,384 grid points.

Fluid transport property

Among the physical parameters, the permeability of the medium k is the most poorly constrained, thus the mobility of the fluid κ or the diffusion coefficient c are difficult to constrain. k varies by several orders of magnitude depending on many factors, such as rock type, conditions of consolidation, and degree of fracturing or damage. It is most likely heterogeneous and is known to show scale dependency (Schulze-Makuch et al. 1999). Accounting for these complexities is beyond the scope of this study. Here, κ was assumed to be uniform in the medium, and a parameter study was conducted.

First, the undrained limit ($\kappa = 0$) was simulated for reference purposes. A sequence of 20 earthquakes was calculated, and the intervals of the 19th and 20th earthquakes were selected as the characteristic timescales of the seismic cycle T_u. Simulations with different κ values were conducted to see the effects of PER. The timescale of PER, T_{PE} is given by an appropriate length scale to

the second power divided by the diffusion coefficient c. Adopting R as the length scale as follows:

$$T_{\mathrm{PE}} = \frac{R^2}{c} = \frac{1}{2}\frac{R^2}{\kappa\mu}\frac{\alpha^2(1-\nu_{\mathrm{u}})(1-2\nu_{\mathrm{d}})^2}{(\nu_{\mathrm{u}}-\nu_{\mathrm{d}})(1-\nu_{\mathrm{d}})}. \tag{40}$$

Simulations with $T_{\mathrm{PE}}/T_{\mathrm{u}}$ from 10^{-7} to 10^{1} were conducted in the parameter study.

Initial conditions

The distribution of the initial loading on fault τ_0 was selected consistently with a steady-state solution at $V = V_* = V_{\mathrm{pl}}$ and $\tau = \tau_*$ as follows:

$$\tau_* = \tau_0 - \frac{\mu}{2c_{\mathrm{s}}}V_{\mathrm{pl}}. \tag{41}$$

Initial perturbations in the state variables are given as follows:

$$\theta(x,0) = 10\left(1+0.1\frac{x}{R}\right)(\text{aging law}), \tag{42}$$

$$\Theta(x,0) = A\left(1+0.1\frac{x}{R}\right)(\text{slip law}). \tag{43}$$

The fault was initially stronger than in the steady-state solution to generate the first events shortly after the start of the simulation. Mirror symmetry at $x = 0$ was broken in the initial state to avoid perfectly symmetric solutions that are unstable. If numerical error including inevitable round-off error is controlled perfectly symmetric, then a numerical solution for a symmetric problem is symmetric. However, if numerical error is not symmetric, then the anti-symmetric component may grow and a numerical solution deviates from the symmetric solution unless it is stable. Because we are interested in a stable solution (attractor), there is no point simulating the growth of the numerical error from a very small amplitude.

Results

For presentation purposes, the length scale was set as $R = 1$ km in visualizing the results, which yielded $L^{\mathrm{ag}} = 1.73$ mm and $L^{\mathrm{sl}} = 2.00$ mm. If a reader is interested in a longer/shorter fault by a factor, the conversion is easily achieved by multiplying by the same factor the values having dimension of length (e.g., fault length and slip) and time, that is, the length times the speed (e.g., event intervals).

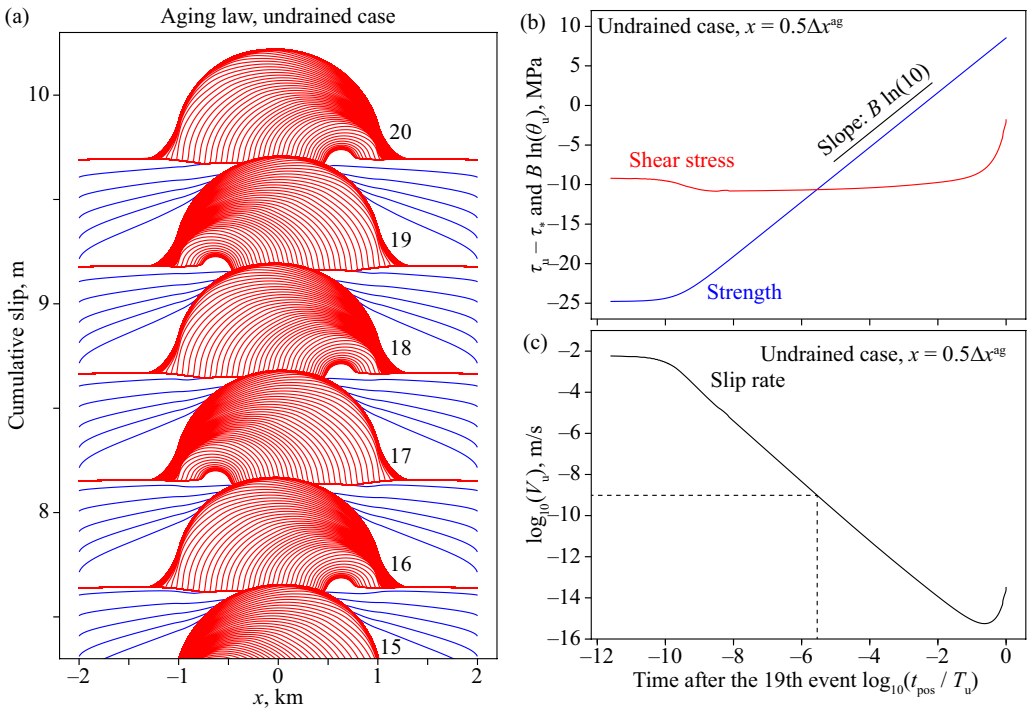

Fig. 5 Simulation result in the undrained case with the aging law. For presentational purposes, the length scale is selected as $R = 1$ km. **a** Cumulative slip distribution, blue: every 10^8 s, red: every 0.02 s during earthquakes. Integers indicate ordinal numbers of earthquakes in the simulated sequence. **b** Shear stress (red) and strength (bule) of the fault relative to the reference at $x = 0.5\Delta x^{\mathrm{ag}} = R/256$ as a function of time after the 19th earthquake. **c** Slip rate near the center, $x = 0.5\Delta x^{\mathrm{ag}}$ as a function of time after the 19th earthquake

Aging law, undrained case

Figure 5 shows the simulation results for the undrained case. Seismic events are defined by a threshold of 0.1 m/s in the spatially maximum slip rate. Coseismic slip distributions are indicated by red lines in Fig. 5a, and there was almost no gap between earthquakes in the central part of the rate-weakening patch. In the core of the seismogenic patch, the seismic coupling was almost one, and significant afterslip did not occur. Although the location of earthquake nucleation alternated between the positive and negative x sides of the patch, the recurrence interval decays to a stable value of $T_u = 5.13 \times 10^8$ s. The elastodynamic time window $t_w = 4$ s corresponds to $7.80 \times 10^{-9}\, T_u$.

Figure 5b shows the interseismic shear stress and fault strength relative to the reference $\tau_u - \tau_*$ and $B\ln(\theta_u)$ at the center ($x = 0.5\Delta x$) as a function of time after the 19th earthquake t_{pos}. The subscript $_u$ indicates the solution in the undrained case, and $t_{pos} = 0$ is defined by a threshold at the spatially maximum slip rate of 0.1 m/s. Equation (27) indicates that $\ln(V)$ is proportional to the stress minus strength, $(\tau_u - \tau_*) - B\ln(\theta_u)$ (Fig. 5c). Thus, the comparison of $\tau_u - \tau_*$ and $B\ln(\theta_u)$ helps us to understand the mechanism of acceleration and deceleration of the fault (Fig. 5c). After the 19th earthquake, V_u was still sufficiently large, even below the threshold, to decrease τ_u in the patch until approximately $t_{pos} = 10^{-9} T_u$. Then, τ_u at the center increased due of aseismic slip outside the locked patch and penetration of creep fronts into it, significantly after about $t_{pos} = 10^{-1} T_u$. $B\ln(\theta_u)$ shows a log-t increase with the slope of $B\ln(10)$, which is characteristic of the aging law in the limit of zero slip rate after the cut-off time due to initially non-zero θ_u. During the interseismic period, V_u varied by more than 10 orders of magnitude. The change in $\ln(V_u)$ was first dominated by the change in strength before t_{pos}/T_u becomes a good fraction of 1, and then by a change in stress. The increase in $B\ln(\theta_u)$ leads to the deceleration of the fault, and V_u becomes smaller than the long-term slip rate $V_{pl} = 10^{-9}$ m/s at $t_{pos} = 2.86 \times 10^{-6} T_u$.

Aging law, effect of PER

The recurrence interval of the undrained case $T_u = 5.13 \times 10^8$ s and Eq. (40) yielded $\kappa = k/\eta = 1.75 \times 10^{-14} (T_{PE}/T_u)^{-1} \mathrm{m}^2/\mathrm{Pas}$. For a typical value of water viscosity $\eta = 10^{-4}$ Pas, $k = 1.75 \times 10^{-18} (T_{PE}/T_u)^{-1} \mathrm{m}^2$. The investigated range

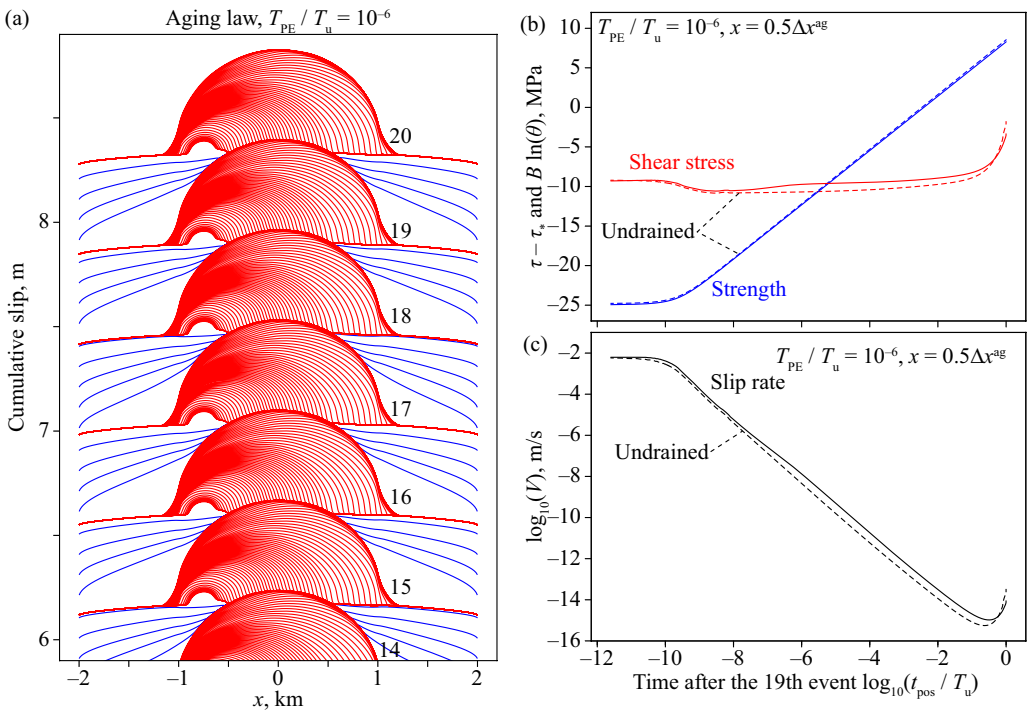

Fig. 6 Example simulation with PE for a fault governed by the aging law. **a** Cumulative slip distribution, blue: every 10^8 s, red: every 0.02 s during earthquakes. Integers indicate ordinal numbers of earthquakes in the simulated sequence. **b** Shear stress (red) and strength (bule) of the fault relative to the reference at $x = 0.5\Delta x^{ag} = R/256$ as a function of time after the 19th earthquake. **c** Slip rate near the center, $x = 0.5\Delta x^{ag} = R/256$ as a function of time after the 19th earthquake

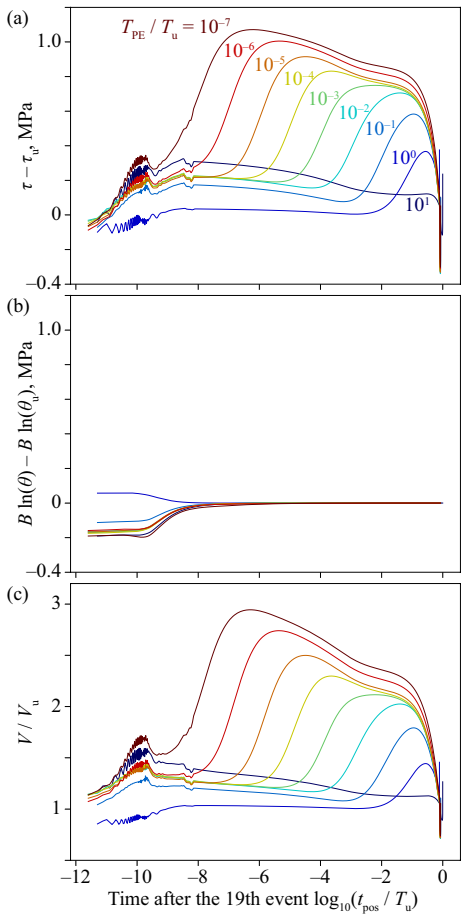

Fig. 7 Effect of PE at $x = 0.5\Delta x^{ag}$ with the aging law and various fluid mobility as a function of the time after the 19th earthquake. Poroelastic diffusion time $T_u = R^2/c$ is indicated by color as shown in **a**. **a** Shear stress, **b** shear strength, and **c** Slip rate relative to the undrained case

of T_{PE}/T_u from 10^{-7} to 10^{1} corresponds to the range of k from 1.75×10^{-11}m^2 to 1.75×10^{-19}m^{-2}.

An example of the simulation result with PER ($T_{PE} = 10^{-6}T_u$) is shown in Fig. 6. It is apparent from the plot of cumulative slip (Fig. 6a) that there was no significant afterslip in the middle of the rate-weakening patch. This was the instance for all simulations conducted.

The evolution of the fault strength $B\ln(\theta)$ almost traces that in the undrained case, while $\tau - \tau_*$ increased at approximately $t_{pos} = 10^{-7}T_u = 0.1T_{PE}$ by approximately 1MPa. The PER loaded the fault in the post-seismic period, but the amplitude was not sufficient to enhance the afterslip significantly. Because $A = 1$MPa, the additional loading due to PER increased V by a factor of 3 (Fig. 6c), and this effect persisted until the next earthquake. Despite an increase in V, the time-dependent strengthening without slip increment (the first term in Eq. (27)) dominated, such that PER did not affect θ.

Cases with different T_{PE} are compared in Fig. 7. The stress buildup due to PER occurred at approximately $t_{pos} = 0.1T_{PE}$, and its amplitude was smaller for a larger T_{PE} (Fig. 7a). With $T_{PE} = 10^{1}T_u$, PER required a longer time than the recurrence interval of the earthquake, and its effect was hardly recognized. The effect of PER on the fault strength $B\ln(\theta)$ is not clear (Fig. 7b), and thus the effect on the slip rate (Fig. 7c) is explained by that in τ.

Slip law, undrained case

The undrained case with the slip law is shown in Fig. 7. Although L at a low slip rate was longer than in the aging law, the nucleation size was much smaller (Ampuero and Rubin 2008). Similar to the case with the aging law, the afterslip was difficult to recognize in Fig. 8a. The recurrence interval was $T_u = 4.71 \times 10^8$ s. The elastodynamic time window $t_w = 4$ s corresponds to $8.49 \times 10^{-9}\ T_u$.

The evolution of the stress relative to the reference $\tau_u - \tau_*$ (Fig. 8b) is similar to that in the case with the aging law (Fig. 5b): $\tau_u - \tau_*$ decreased until approximately $t_{pos} = 10^{-9}T_u$, and then increased significantly after approximately $t_{pos} = 10^{-1}T_u$. The fault strength Θ_u showed a log-t increase, even though it was not predicted in the limit of $V \to 0$ (Eq. (28)). The evolution of Θ_u requires a slip increment for the slip law. The strengthening rate was smaller than $B\ln(10)$, as mentioned by Marone (1998) in the context of a slide-hold-slide friction experiment. V_u decreased with time more slowly than in the case of the aging law and became smaller than V_{pl} at $t_{pos} = 4.81 \times 10^{-4}T_u$. It continued to decrease until t_{pos} became a good fraction of T_u, and increased thereafter (Fig. 8c). Θ_u also increased sharply during this acceleration period.

Slip law, effect of PER

The recurrence interval $T_u = 4.71 \times 10^8$ s, Eq. (40), and $\eta = 10^{-4}$ Pas yield $k = 1.91 \times 10^{-18}(T_{PE}/T_u)^{-1}$m^2. The investigated range of T_{PE}/T_u from 10^{-7} to 10^{1} corresponds to the range of k from 1.91×10^{-11}m^2 to 1.91×10^{-19}m^{-2}.

An example case with the slip law and PER ($T_{PE} = 10^{-6}T_u$) is shown in Fig. 9, on the same vertical scale as that with the aging law (Fig. 6). Again, afterslip was hardly visible in the plot of the cumulative slip (Fig. 9a). This was the instance for all simulations conducted. Therefore, the present simulations do not support significant afterslip in the core of the seismogenic patch due to PER for the slip law or for the aging law.

$\tau - \tau_*$ increased due to PER by approximately 1 MPa at approximately $t_{pos} = 0.1T_{PE}$, and Θ also increased relative to the undrained case almost at the same time

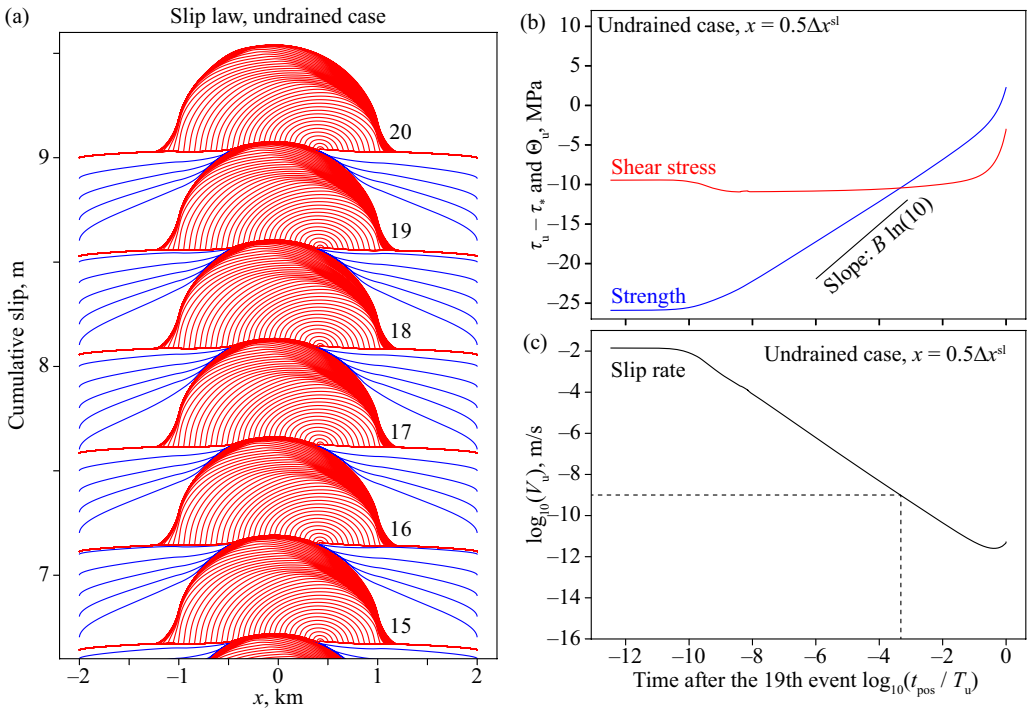

Fig. 8 Simulation result in the undrained case with the slip law. For presentational purposes, the length scale is selected as $R = 1$ km. **a** Cumulative slip distribution, blue: every 10^8 s, red: every 0.02 s during earthquakes. Integers indicate ordinal numbers of earthquakes in the simulated sequence. **b** Shear stress (red) and strength (bule) of the fault relative to the reference at $x = 0.5\Delta x^{\mathrm{sl}} = R/2048$ as a function of time after the 19th earthquake. **c** Slip rate near the center, $x = 0.5\Delta x^{\mathrm{sl}}$ as a function of time after the 19th earthquake

(Fig. 9b). PER increased V (Fig. 9c), but this effect was minor compared to the case with the aging law (Fig. 6c) owing to the increase in Θ.

Cases with different T_{PE} are compared in Fig. 10. Loading due to PER increased τ at approximately $t_{\mathrm{pos}} = 0.1T_{\mathrm{PE}}$ (Fig. 10a). When $T_{\mathrm{PE}} = 10^1 T_{\mathrm{u}}$, PER did not affect τ significantly. Θ also increased at approximately $t_{\mathrm{pos}} = 0.1T_{\mathrm{PE}}$ by a smaller but comparable amount (Fig. 10b). Consequently, the increase in V relative to the undrained case was only modest (Fig. 10c).

Discussion

The series of simulations conducted in this study indicate that PER causes postseismic loading to the patch of coseismic slip, but the enhancement of afterslip due to PER is negligible. In the idealized case of uniform stress drop and constant frictional strength (Fig. 1), the afterslip normalized by the coseismic slip is $\mu_{\mathrm{u}}'/\mu_{\mathrm{d}}' - 1 = (1-\nu_{\mathrm{d}})/(1-\nu_{\mathrm{u}}) - 1 = 1.36 \times 10^{-1}$. Compared to this, Figs. 6a and 8a clearly show that the postseismic healing of a fault efficiently suppresses the afterslip at the center of the rate-weakening patch. This is the case not only in cases with the aging law but also with the slip law. The simulation results were consistent with the absence of afterslip inside the coseismic slip patches in observation.

Marone et al. (1995) inferred a very long cut-off healing time of approximately 100days $\approx 10^7$ s based on the observation of small repeating earthquakes. The long cut-off time delays healing and may produce afterslip due to PER. However, by what means to realize such a long cut-off time in RSF is an open question. In the aging law, the cut-off time is given by L divided by the coseismic slip rate well behind the rupture front. Stress drop $\Delta\sigma$ of 3MPa and the impedance of μ/c_{s} of 10 MPa(m/s)$^{-1}$ yields coseismic slip rate of the order of 0.1 m/s in self-similar dynamic rupture (Broberg 1978). For a cut-off time of 10^7 s, L must be on the order of 10^6 m. Evidently, the nucleation size (Eq. (31)) is too large to model a realistic earthquake.

The intrinsic cut-off time of the state evolution t_{cx} (Nakatani and Scholz 2006) may also produce a long cut-off time. If it is implemented in the aging law, the friction law becomes as follows:

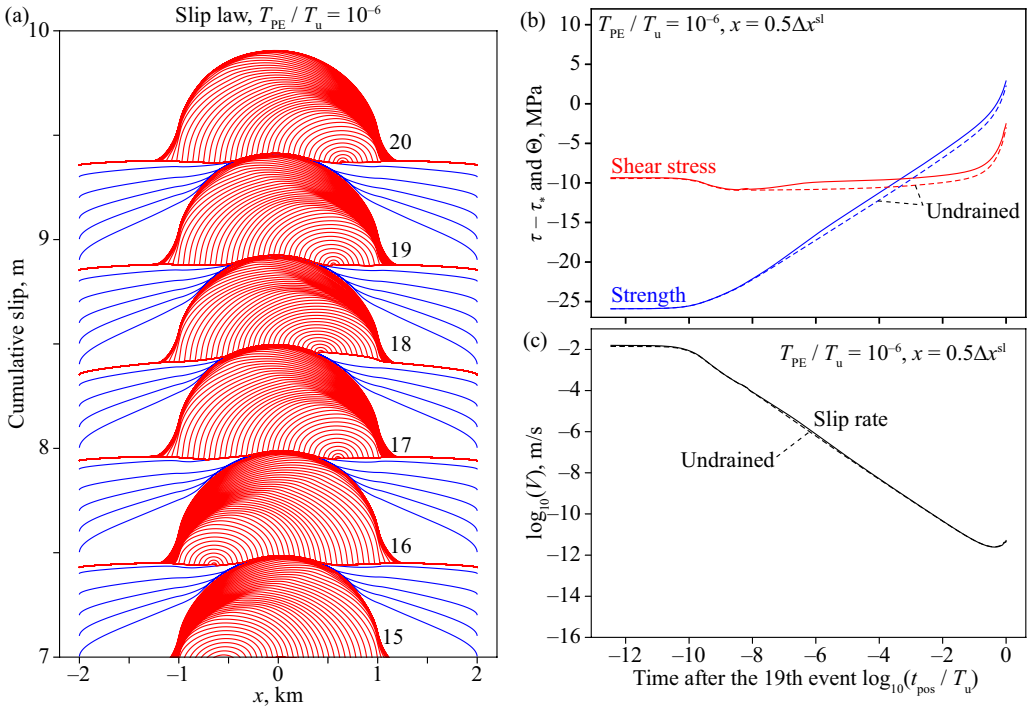

Fig. 9 Example simulation with PE for a fault governed by the aging law. **a** Cumulative slip distribution, blue: every 10^8 s, red: every 0.02 s during earthquakes. Integers indicate ordinal numbers of earthquakes in the simulated sequence. **b** Shear stress (red) and strength (bule) of the fault relative to the reference at $x = 0.5\Delta x^{sl} = R/2048$ as a function of time after the 19th earthquake. **c** Slip rate near the center, $x = 0.5\Delta x^{sl}$ as a function of time after the 19th earthquake

$$\begin{aligned} \tau &= \tau_* + A\ln\left(\frac{V}{V_*}\right) + B\ln(\theta + 1) \\ \dot{\theta} &= \frac{V}{L}\left(\frac{V_*}{V} - \theta\right) \\ V_* &= L/t_{cx} \end{aligned} . \tag{44}$$

The steady-state shear strength is given as follows:

$$\tau_{ss} = \tau_* + A\ln\left(\frac{Vt_{cx}}{L}\right) + B\ln\left(\frac{L}{Vt_{cx}} + 1\right), \tag{45}$$

and the rate dependency, as follows:

$$\frac{d\tau_{ss}}{d\ln(V)} = A - \frac{B}{1 + Vt_{cx}/L}. \tag{46}$$

Therefore, the friction law becomes rate strengthening at $V > (B/A + 1)L/t_{cx} \equiv V_c$. Laboratory-measured values of $L < 1$ mm (e.g., Blanpied et al. 1998) and the large cutoff time $t_{cx} \approx 10^8$ s yield $V_c < 10^{-11}$ m/s, which is too small for frictional instability to occur at typical long-term slip rate. The reconciliation of the long cut-off time and seismogenic fault behavior deserves future study.

Conclusions

Quasistatic poroelasticity (PE) was successfully implemented in a dynamic earthquake sequence simulation for a fault governed by a rate- and state-dependent friction law (RSF) using a spectral boundary integral equation method. In this method, the numerical approximation of the time dependency of Green's function in the wavenumber domain and the definition of memory variables are the keys to avoid temporal convolution for PE. The additional computational cost relative to the elastic simulation was negligible. A simple model of a planar fault with a rate-weakening patch embedded in a rate-strengthening region was simulated to investigate the effects of poroelastic rebound (PER). As for the RSF, not only the aging law, but also the slip law is investigated with modifications to increase the characteristic state-evolution slip distance at coseismic slip rates for tractability of the numerical simulation. The simulation results indicate that PER causes postseismic loading to the region of stress drop of approximately $0.1R^2/c$ after

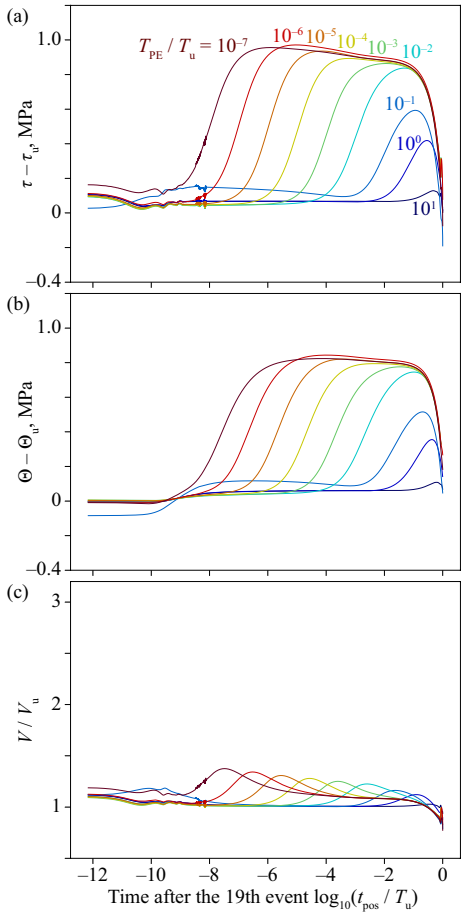

Fig. 10 Effect of PE at $x = 0.5\Delta x^{sl}$ with the slip law and various fluid mobility as a function of the time after the 19th earthquake. Poroelastic diffusion time $T_u = R^2/c$ is indicated by color as shown in **a**. **a** Shear stress, **b** shear strength, and **c** Slip rate relative to the undrained case

an earthquake, where R is the half length of the coseismic slip patch and c is the diffusivity of the pore fluid pressure. For both the aging law and slip law, however, the healing of a fault efficiently suppresses afterslip inside a coseismic slip patch, while it was suggested by previous theoretical studies for a crack of constant strength. The simulation results are consistent with the absence of afterslip within the coseismic slip patches in the observations. When the cases with the two different friction laws are compared, healing is more significant in the cases with the aging law, but the effect of PER on the slip rate V is minor in the cases with the slip law. In the interseismic period, the log-t healing term is dominant for the aging law. Therefore, the change in V hardly affects the evolution of the fault strength. On the other hand, for the slip law, healing is driven by the slip increment, and thus the increase in V results in additional strengthening, which works as a negative feedback.

Abbreviations

FFT: Fast Fourier transformation; ODE: Ordinary differential equation; PE: Poroelasticity; PER: Poroelastic rebound; RSF: Rate- and state-dependent friction law; SBIEM: Spectral boundary integral equation method.

Acknowledgements

The author would like to thank Y. Iio for a discussion useful in motivating the present study and T. Nishimura for a discussion on the interpretation of geodetic inversion results. Two reviewers (P. Romanet and E. R. Heimisson) gave very useful comments in improving the manuscript. In the review process, Heimisson informed the author of his manuscript and an online preprint on a similar problem submitted to JGR on the same day with the present paper.

Author contributions

HN developed the present method, coded the simulation program, analyzed the results, and composed the original draft. The author read and approved the final manuscript.

Funding

The present study was supported by the Ministry of Education, Culture, Sports, Science and Technology (MEXT) of Japan under its Second Earthquake and Volcano Hazards Observation and Research Program (Earthquake and Volcano Hazard Reduction Research) and by JSPS KAKENHI Grant Numbers 21H05201, 19K04038.

Availability of data and materials

No observational data were used for this study. The simulation code used in this study is available upon reasonable request to the author.

Declarations

Ethics approval and consent to participate

Not applicable.

Consent for publication

Not applicable.

Competing interests

The author does not have any competing interests.

Received: 8 February 2022 Accepted: 16 May 2022
Published online: 09 June 2022

References

Ampuero J-P, Rubin AM (2008) Earthquake nucleation on rate and state faults—aging and slip laws. J Geophys Res 113:B01302. https://doi.org/10.1029/2007JB005082

Andrews DJ (2004) Rupture models with dynamically determined breakdown displacement. Bull Seismol Soc Am 94:769–775. https://doi.org/10.1785/0120030142

Blanpied ML, Marone CJ, Lockner DA, Byerlee JD, King DP (1998) Quantitative measure of the variation in fault rheology due to fluid-rock interactions. J Geophys Res Solid Earth 103:9691–9712. https://doi.org/10.1029/98JB00162

Broberg KB (1978) On transient sliding motion. Geophys J Int 52:397–432. https://doi.org/10.1111/j.1365-246X.1978.tb04240.x

Chen T, Lapusta N (2009) Scaling of small repeating earthquakes explained by interaction of seismic and aseismic slip in a rate and state fault model. J Geophys Res Solid Earth 114:B01311. https://doi.org/10.1029/2008JB005749

Cheng AH-D, Detournay E (1998) On singular integral equations and fundamental solutions of poroelasticity. Int J Solids Struct 35:4521–4555. https://doi.org/10.1016/S0020-7683(98)00082-1
Cochard A, Madariaga R (1994) Dynamic faulting under rate-dependent friction. Pure Appl Geophys 142:419–445. https://doi.org/10.1007/BF00876049
Cochard A, Rice JR (1997) A spectral method for numerical elastodynamic fracture analysis without spatial replication of the rupture event. J Mech Phys Solids 45:1393–1418
Detournay E, Cheng AH-D (1991) Plane strain analysis of a stationary hydraulic fracture in a poroelastic medium. Int J Solids Struct 27:1645–1662. https://doi.org/10.1016/0020-7683(91)90067-P
Di Toro G, Han R, Hirose T, De Paola N, Nielsen S, Mizoguchi K, Ferri F, Cocco M, Shimamoto T (2011) Fault lubrication during earthquakes. Nature 471:494–498. https://doi.org/10.1038/nature09838
Dieterich JH (1972) Time-dependent friction in rocks. J Geophys Res 77:3690–3697. https://doi.org/10.1029/JB077i020p03690
Dieterich JH (1979) Modeling of rock friction: 1. Experimental results and constitutive equations. J Geophys Res 84:2161–2168. https://doi.org/10.1029/JB084iB05p02161
Dokos SJ (1946) Sliding friction under extreme pressures—1. J Appl Mech 13:A148–A156. https://doi.org/10.1115/1.4009539
Dunham EM, Rice JR (2008) Earthquake slip between dissimilar poroelastic materials. J Geophys Res 113:B09304. https://doi.org/10.1029/2007JB005405
Geubelle P, Rice JR (1995) A spectral method for three-dimensional elastodynamic fracture problems. J Mech Phys Solids 43:1791–1824. https://doi.org/10.1016/0022-5096(95)00043-I
Heimisson ER, Dunham EM, Almquist M (2019) Poroelastic effects destabilize mildly rate-strengthening friction to generate stable slow slip pulses. J Mech Phys Solids 130:262–279. https://doi.org/10.1016/j.jmps.2019.06.007
Heimisson ER, Rudnicki J, Lapusta N (2021) Dilatancy and compaction of a rate-and-state fault in a poroelastic medium: linearized stability analysis. J Geophys Res. https://doi.org/10.1029/2021JB022071
Hsu YJ, Simons M, Avouac JP, Galetzka J, Sieh K, Chlieh M, Natawidjaja D, Prawirodirdjo L, Bock Y (2006) Frictional afterslip following the 2005 Nias-Simeulue earthquake, Sumatra. Science 312:1921–1926. https://doi.org/10.1126/science.1126960
Jha B, Juanes R (2014) Coupled multiphase flow and poromechanics: a computational model of pore pressure effects on fault slip and earthquake triggering. Water Resour Res 50:3776–3808. https://doi.org/10.1002/2013WR015175
Kato A, Igarashi T (2012) Regional extent of the large coseismic slip zone of the 2011 Mw 9.0 Tohoku-Oki earthquake delineated by on-fault aftershocks. Geophys Res Lett 39:L15301. https://doi.org/10.1029/2012GL052220
Knopoff L (1958) Energy release in earthquakes. Geophys J Roy Astron Soc 1:44–52. https://doi.org/10.1111/j.1365-246X.1958.tb00033.x
Lapusta N, Liu Y (2009) Three-dimensional boundary integral modeling of spontaneous earthquake sequences and aseismic slip. J Geophys Res 114:B09303. https://doi.org/10.1029/2008JB005934
Lapusta N, Rice JR, Ben-Zion Y, Zheng G (2000) Elastodynamic analysis for slow tectonic loading with spontaneous rupture episodes on faults with rate- and state-dependent friction. J Geophys Res Solid Earth 105(23765–23789):789. https://doi.org/10.1029/2000JB900250
Marone C (1998) Laboratory-derived friction laws and their application to seismic faulting. Annu Rev Earth Planet Sci 26:643–696. https://doi.org/10.1146/annurev.earth.26.1.643
Marone C, Vidale JE, Ellsworth WL (1995) Fault healing inferred from time dependent variations in source properties of repeating earthquakes. Geophys Res Lett 22:3095–3098. https://doi.org/10.1029/95GL03076
Meneses-Gutierrez A, Nishimura T, Hashimoto M (2019) Coseismic and postseismic deformation of the 2016 central Tottori earthquake and its slip model. J Geophys Res Solid Earth 124:2202–2217. https://doi.org/10.1029/2018JB016105
Miyake Y, Noda H (2019) Fully dynamic earthquake sequence simulation of a fault in a viscoelastic medium using a spectral boundary integral equation method: does interseismic stress relaxation promote aseismic transients? Earth, Planets and Space 71:137. https://doi.org/10.1186/s40623-019-1113-8
Miyazaki S, Segall P, Fukuda J, Kato T (2004) Space time distribution of afterslip following the 2003 Tokachi-oki earthquake: implications for variations in fault zone frictional properties. Geophys Res Lett 31:L06623. https://doi.org/10.1029/2003GL019410
Nakatani M, Scholz CH (2006) Intrinsic and apparent short-time limits for fault healing: theory, observations, and implications for velocity-dependent friction. J Geophys Res Solid Earth 111:B12208. https://doi.org/10.1029/2005JB004096
Noda H (2021) Dynamic earthquake sequence simulation with a SBIEM without periodic boundaries. Earth, Planets and Space 73:137. https://doi.org/10.1186/s40623-021-01465-6
Noda H, Hori T (2014) Under what circumstances does a seismogenic patch produce aseismic transients in the later interseismic period? Geophys Res Lett 41:7477–7484. https://doi.org/10.1002/2014GL061676
Noda H, Lapusta N (2010) Three-dimensional earthquake sequence simulations with evolving temperature and pore pressure due to shear heating: effect of heterogeneous hydraulic diffusivity. J Geophys Res 115:B12314. https://doi.org/10.1029/2010JB007780
Peltzer G, Rosen P, Rogez F, Hudnut K (1996) Postseismic rebound in fault step-Overs caused by pore fluid flow. Science 273:1202–1204. https://doi.org/10.1126/science.273.5279.1202
Rice JR (1993) Spatio-temporal complexity of slip on a fault. J Geophys Res 98:9885–9907. https://doi.org/10.1029/93JB00191
Rice JR, Ben-Zion Y (1996) Slip complexity in earthquake fault models. Proc Natl Acad Sci USA 93:3811–3818
Rubin AM, Ampuero J-P (2005) Earthquake nucleation on (aging) rate and state faults. J Geophys Res 110:B11312. https://doi.org/10.1029/2005JB003686
Rudnicki JW, Rice JR (2006) Effective normal stress alteration due to pore pressure changes induced by dynamic slip propagation on a plane between dissimilar materials. J Geophys Res 111:B10308. https://doi.org/10.1029/2006JB004396
Ruina A (1983) Slip instability and state variable friction laws. J Geophys Res Solid Earth 88(10359–10370):370. https://doi.org/10.1029/JB088iB12p10359
Scholz CH (1998) Earthquakes and friction laws. Nature 391:37–42. https://doi.org/10.1038/34097
Schulze-Makuch D, Carlson DA, Cherkauer DS, Malik P (1999) Scale dependency of hydraulic conductivity in heterogeneous media. Ground Water 37:904–919. https://doi.org/10.1111/j.1745-6584.1999.tb01190.x
Song Y, Rudnicki JW (2017) Plane-strain shear dislocation on a leaky plane in a poroelastic solid. J Appl Mech 84:021008. https://doi.org/10.1115/1.4035179
Torberntsson K, Stiernström V, Mattsson K, Dunham EM (2018) A finite difference method for earthquake sequences in poroelastic solids. Comput Geosci 22:1351–1370. https://doi.org/10.1007/s10596-018-9757-1
Tse ST, Rice JR (1986) Crustal earthquake instability in relation to the depth variation of frictional slip properties. J Geophys Res 91:9452–9472. https://doi.org/10.1029/JB091iB09p09452
Wang H (2001) Theory of Linear Poroelasticity with Applications to Geomechanics and Hydrogeology. Princeton Series in Geophysics 2. Princeton University Press, Princeton
Yamashita T (2007) Postseismic quasi-static fault slip due to pore pressure change on a bimaterial interface. J Geophys Res. https://doi.org/10.1029/2006JB004667
Yamashita T, Suzuki T (2009) Quasi-static fault slip on an interface between poroelastic media with different hydraulic diffusivity: a generation mechanism of afterslip. J Geophys Res. https://doi.org/10.1029/2008JB005930

Publisher's Note